Surface microseismic imaging in the presence of high velocity lithological layers

David Price∗, Doug Angus∗, Kit Chambers†, and Glenn Jones‡

∗*School of Earth & Environment, University of Leeds, Leeds, UK,* †*Pinnacle - a Halliburton service, Cornwall, UK* ‡*Pinnacle - a Halliburton service, Cornwall, UK, now at Department of mechanical engineering, Imperial College London, UK*

(July 8, 2015)

Running head: **Surface Microseismic Imaging**

ABSTRACT

Surface microseismic monitoring above regions containing high velocity units will be influenced by a reduction in the effective array aperture and contain significant seismic coda due to an increase in reflected and converted wave energy which can influence the capability of surface arrays to image microseismic events. We examine the imaging difficulties due to reduction of effective array aperture and increased coda within microseismic data caused by the presence of a fast anhydrite layer. We generate and use finite-difference, full waveform microseismic synthetics derived from one-dimensional sonic log data taken from an unconventional shale reservoir in complex anhydrite geology. Two imaging techniques are used to locate the synthetic microseismic events. A simplistic and easily reproducible Standard Diffraction Imaging (SDI) procedure and a more sophisticated technique, Moment Tensor Microseismic Imaging™ (MTMI™). We confirm that the presence of high velocity layers, such as anhydrite, reduces the overall aperture of a surface array, which results in poor resolution of imaged events and reduction in accuracy of event locations. More im-

portantly, we demonstrate that coda in the microseismic data can isolate itself from the direct arrival, stack into the final imaging result and be misinterpreted as separate events located directly below the true source location, which is unavoidable given the ambiguity between event location and time. Comparison of the two imaging procedures show that even though the more sophisticated MTMI was able to better cope with the effects caused by high velocity layers, it still demonstrated a significant reduction in resolution of imaged events, a reduction in accuracy and evidence of multiple and converted energy still present in the final imaging result.

LIST OF FIGURES

puted using an array length of 4km with 100m receiver spacing. Results are presented for SDI, MTMI P-wave only imaging and MTMI P- and S-wave imaging. All images produced using the same procedure as that for Figure 3.

7   Comparison of microseismic imaging due to variable receiver spacing. Results show SDI and MTMI image function for receiver spacings of 20m, 100m and 200m for simples models A and B. All images produced using the same procedure as that for Figure 3.

8   Comparison of microseismic imaging due to variable receiver spacing. Results show SDI and MTMI image function for recever spacings of 20m, 100m and 200m for complex models C and D. All images produced using the same procedure as that for Figure 3.

9   Comparison of microseismic imaging due to variable source offset. Results show SDI and MTMI image function for source offset of 0km, 1km and 2km from the centre of the array for simple models A and B. Total array length of 6km used for this test with 100 receiver spacing. All images produced using the same procedure as that for Figure 3.

10   Comparison of microseismic imaging due to variable source offset. Results show SDI and MTMI image function for source offset of 0km, 1km and 2km from the centre of the array for complex models C and D. Total array length of 6km used for this test with 100 receiver spacing. All images produced using the same procedure as that for Figure 3.

11   Velocity models (P-wave = blue line and S-wave = red line) with their respective vertical component microseismic waveforms.

12   SDI and MTMI image functions collapsed in origin time for the velocity models shown in Figure 11

13   MTMI image functions at various origin times for the non-smoothed complex velocity model and the moderately smoothed velocity model shown in Figure 11.

14   1D P- (Blue) and S-wave (Red) velocity models use by Sobion (2014) to create

3D FD microseismic synthetics. Their corresponding SDI and MTMI results are shown as 2D slices of the 3D volume along x and y, taken at the source location. The actual source location is shown by the yellow dot.

LIST OF TABLES

INTRODUCTION

Microseismic monitoring is now regarded as the most widely accepted method for monitoring hydraulic stimulation and is becoming an essential tool for unconventional resource exploitation (e.g., shale-gas). Due to the relatively small magnitude of microseismic events, microseismic monitoring has traditionally involved the temporary deployment of borehole arrays consisting of up to 40 three-component sensors deployed within a lateral distance of less than 500 m from the region of expected microseismicity (e.g., Warpinski, 2009). Traditional techniques to determine source location and origin time involve analysing discrete P- and S-wave arrivals within the raw data (e.g., via triangulation, Gibowicz & Kijko, 1994) and the source mechanism estimated by adequately sampling the source radiation pattern (e.g., Trifu et al., 2000; Vavryčuk, 2007; Šílený, 2009; Baig & Urbancic, 2010; Eisner et al., 2010b). Determining the moment tensor can improve reservoir characterisation as it provides detail on the orientation of fractures, the type of failure (e.g. shear or tensile) and their magnitude (e.g., Baig & Urbancic, 2010; Duncan & Eisner, 2010).

Surface microseismic arrays have now become increasingly popular as they provide greater flexibility in array location and acquisition geometry. This greater flexibility has led to the deployment of large aperture arrays that provide greater fold and increased range of azimuths to the area of interest which aids moment tensor estimation (e.g., Duncan, 2005; Robein et al., 2009; Duncan & Eisner, 2010). However, microseismic signals recorded at the surface are typically at or below the signal-to-noise ratio (e.g., Chambers et al., 2010) due to high noise levels and the relatively large distances between source and receiver. Therefore, traditional borehole monitoring techniques used to determine source location, origin time and mechanism become unfeasible in surface monitoring. Surface array microseismic mon-

itoring often necessitates the use of more advanced acquisition and processing techniques that utilise the features of large aperture arrays to detect weak events in the presence of high background noise and to adequately sample the event focal sphere (e.g., Duncan & Eisner, 2010).

Recent surface microseismic monitoring above regions containing high velocity units, such as anhydrite in sub-salt environments, have shown unexpected imaging results that have raised concern over the current imaging capability of surface arrays (e.g., Figure 1 and Price, 2013). A layer with a relatively high seismic velocity compared to its surrounding rock results in a strong impedance contrast at the boundary between the two rock types. For surface microseismic arrays, large impedance contrasts can lead to (i) strong defocussing of upward propagating seismic energy leading to degradation of subsurface illumination, and (ii) increase in multiply reflected and converted wave energy within the microseismic data.

Many current and prospective unconventional shale reserves occur in the presence of high-velocity layers such as evaporite (e.g., Börner, 2003; EIA, 2013). For example, the Permian Zechstein basin of NW-Europe, Amadeus Basin of Northern Australia, Permian basin of southern USA and the Elk basin of Southern Canada all contain lithologicaly fast evaporite layers such as dolomite, anhydrites and salt (e.g., Benson & Davis, 2000; Campbell, 1987; Christie-Black & Driscoll, 19956; Mapstone & Mcilroy, 2006; Sloss, 1959). Therefore, the ability to image events in their presence will be essential for surface micro-seismic development.

In this paper, we explore the influence of a high velocity layer on surface microseismic imaging, specifically the impact of anhydrite on the effective surface array aperture and its contribution to the presence of multiply reflected and converted (scattered) wave energy.

We do so by comparing microseismic imaging results for a suite of full-waveform synthetic data representing a typical surface monitoring scenario using one-dimensional (1D) velocity models adapted from an unconventional reservoir that sits beneath a lithologically fast anhydrite layer. Two different imaging processes are tested on each dataset; A simplistic and easily reproducible Standard Diffraction stack Imaging (SDI) procedure (McMechan, 1982; Kochnev et al., 2007; Chambers et al., 2010) and a more sophisticated process, Moment Tensor Microseismic Imaging (MTMI) (Chambers et al., 2014).

SURFACE MICROSEISMIC IMAGING METHODS

Surface array location methods do not require specific arrival time picks of P- and S-wave signals but utilise the attributes of surface arrays, such as large aperture and increased fold, to locate events even in the presence of high background noise. They use a procedure similar to that of diffraction stack migration (e.g., Kirchhoff migration) to align arrivals from specified locations within the subsurface. This coherence based imaging technique generally involves finding a point in space and time that maximises a stacking function, known as microseismic imaging (e.g., McMechan, 1982; Kochnev et al., 2007; Chambers et al., 2010; Duncan & Eisner, 2010; Chambers et al., 2014). In this paper we classify migration style algorithms within two end-member approaches, either a *diffraction stack* approach or a *reverse time imaging* approach.

The diffraction stack approach (e.g., Chambers et al., 2010; Duncan & Eisner, 2010; Drew et al., 2013) work via a summation of amplitudes along hyperbolic trajectories with curvature governed by the given velocity model (Yilmaz & Doherty, 1987). This amplitude summation is known as stacking and is computed using the data from each receiver seismogram sampled at a time consistent with that of the estimated arrival time from a specified

image point. The procedure is then repeated for each image point and origin time and a stack (or image) function is formed.

The reverse time imaging approach makes use of the reversibility of wave equations to numerically back propagate a recorded seismogram through a known velocity field allowing the energy of a recorded wave to be propagated backwards in time towards its source (e.g., McMechan, 1982; Gajewski & Tessmer, 2004; Xuan & Sava, 2010; Artman et al., 2010; Chambers et al., 2014). Using the concept of the *exploding reflector model* (e.g., Claerbout, 1982), each time step is considered an equivalent source to the recorded seismogram signal and continued propagation of the wave-field backwards in time will eventually result in the energy being focused at the source location. However, this approach is more computationally expensive than its diffraction counterpart (Chambers et al., 2010; Angus et al., 2014).

Both Standard Diffraction (SDI) and reverse time imaging suffer from the characteristic radiation pattern of microseismic events. The polarity of both P- and S-wave first arrivals for non-volumetric failure mechanisms differ depending on the location of observation within the focal sphere. If the polarity of the arrival changes across the array, then SDI techniques produce a complex image; because true physical signals destructively interfere during stacking (e.g., in an extreme case a microseismic event can appear as a null point rather than a desired maxima). Standard reverse time imaging is subject to the same instability, where this anisotropic radiation pattern can yield multiple maxima within the imaging domain and hence reduce event detectability (Chambers et al., 2014). Several approaches have been developed to compensate for this complex image problem (e.g., Özbek et al., 2013; Anikiev et al., 2014), however, these techniques are often computationally expensive or are subjected to factors that produce biased results (Chambers et al., 2014).

Chambers et al. (2014) has developed a new imaging method that combines moment tensor reverse time imaging with standard diffraction imaging. The MTMI process simultaneously solves for the source location and the corresponding moment tensor components as in conventional moment tensor imaging (e.g., O'Toole & Woodhouse, 2011), but with the computational speed and efficiency of the diffraction stack approach.

SYNTHETIC MICROSEISMIC DATA

For this study we compute full-waveform microseismic synthetics using the Finite-Difference (FD) algorithm E3D (Larsen & Harris, 1993). Due to typical dimensions of a monitoring volume (e.g., Duncan & Eisner, 2010; Chambers et al., 2010), and our sole focus of high-velocity lithological contrasts we reduce our problem to 2D isotropic. However, it should be noted that reducing the problem from 3D to 2D decreases the accuracy of the computed synthetics (e.g., Liner, 2004) as amplitude decay in 2D simulation's are proportional to $1/\sqrt{r}$ compared to that of $1/r$ for 3D. This simplification can be problematic if significant lateral heterogeneity is expected or if absolute amplitudes are required (e.g., for moment magnitude calculation). However, as our velocity models are one dimensional and we are concerned only with relative amplitude and waveform perturbations expressed in the radiation pattern, reduction to 2D for this study can be justified. We demonstrate later that the 2D assumption does not render our conclusions invalid by comparing imaging results from a 3D FD solution (Xu, 2011) for similar 1D velocity models (Sobion, 2014).

The 2D model geometry has a lateral (y-axis) dimension of 10.4km and depth (z-axis) of 4.2km with a microseismic point source located at $y = 5.2$km, $z = 3.0$km. The source mechanism is that of a vertical strike slip fault defined by the moment tensor $M_{yz} = -1$, $M_{xx} = M_{yy} = M_{zz} = M_{xy} = M_{xz} = 0$ (Jost & Herrmann, 1989) whose radiation pattern will

11

highlight instabilities of standard imaging algorithms. A moment magnitude of $M_w = -2$ (i.e., seismic moment $M_o = 1.26 \times 10^{13}$dyne/cm) is chosen as this is representative of a typical microseismic event detectable at the surface (e.g., Warpinski et al., 2012). For an event with moment magnitude $M_w = -2$, the dominant microseismic source frequencies measured by surface arrays would be anywhere between 10Hz and 100Hz (e.g., Eisner et al., 2013) depending on subsurface attenuation effects and typical geophone sensitivities.

Absorbing boundary conditions are applied to the sides and bottom of the grid, and a free surface applied to the top boundary (equivalent to air-rock boundary). In addition, a high attenuation zone, 200m thick, is applied along the sides and bottom to ensure no energy is reflected back into the model. A total of 501 two-component (horizontal component y and vertical component z) receivers are placed along the surface outside of the high attenuating zone between 0.2km and 10.2km with 20m spacing. Based on dispersion (minimum of 10 grid points per minimum wavelength) and stability requirements (e.g., Alford et al., 1974; Kelly et al., 1976), the spatial (Δh) and temporal (Δt) grid increments for a 100Hz dominant frequency event are $\Delta h = 0.0001$km and $\Delta t = 0.00001$s, respectively.

While keeping the geometry of the model constant, we generate four 1D velocity models shown in Figure 2. Model D is an actual sonic log taken from an unconventional shale-gas reservoir that sits below anhydrite geology. The remaining three models are adaptations of this true 1D sonic log, model C making use of the general trend of the log, but with suppression of the fast velocity anhydrite layer and models A and B being over simplified versions of complex models C and D unlikely to be observed in nature, but useful to exaggerate SDI and MTMI imaging effects caused by an extreme velocity transition. In each model, the density is computed using the relation of Gardner et al. (1974). Frequency-independent attenuation is incorporated into complex models C and D using the formulae of Waters (1978)

and Udías Vallina (1999) and the dominant source frequency of the Ricker wavelet, in both cases, is chosen to be 100Hz. To keep models A and B as simple as possible, attenuation is not incorporated but to make them comparable to complex models C and D, the dominant source frequency of the Ricker wavelet was chosen to mimic the frequency of the P-wave first arrival seen in the complex models ($\approx$ 70Hz).

RESULTS

Image functions are computed for a condensed 2km $\times$ 2km region of the subsurface ($\Delta y = 4 - 6$km and $\Delta z = 2 - 4$km) and are collapsed in origin time (the maximum stacking value for each image point in time is computed) to provide a suite of 2D images for display purposes. A 2D spatial Gaussian filter (σ_z=50m, σ_y=12.5m) is applied to each collapsed function to smooth the final image and is normalised to range between 0 and 1. The quantitative results are also presented in table format (Table 1) summarising the imaging results in terms of location bias (distance in meters between image maxima and actual source location) and precision (height, Δz, and width, Δy, in meters, of a 75% contour of the normalised collapsed image function). The results section is split into two parts, (1) analysis of effective array geometry (e.g., how the presence of anhydrite effects the aperture, fold and offset requirements of a surface array) and (2) analysis of the effect that multiple reflections and converted (scattered) wave energy has on microseismic imaging. It should be noted that taking a 75% contour of a normalised collapsed image function is not the same as statistically computing an inversion error ellipse, but it does provide a good representation of the resolution of the image peak in terms of its surface area. It should also be noted that location bias values are given to sub-meter precision due to our models being exact.

Effective Array Geometry

Aperture

We consider three surface array lengths of 10km, 6km and 4km (centred over the source location). The receiver spacing for all arrays is chosen to be 100m consistent with real monitoring scenarios. The result of SDI and MTMI imaging using only P-wave arrivals for each of the three array lengths are shown in Figures 3 and 4. A joint P- and S-wave MTMI stack is applied to the 4km array to explore whether using both P- (using vertical component data) and S-wave (using transverse component data) arrivals in the imaging calculation can compensate for a small array aperture (Figure 5). The quantitative results for each imaging procedure are given in Table 1. Although microseismic events recorded with surface arrays typically have peak frequencies anywhere between 10Hz to 100Hz, due to near surface layers having high attenuation and the common occurrence of high frequency noise e.g. electrical (50Hz - 60Hz in the USA and Canada), typically only the low frequency (10Hz - 30Hz) part of the direct arrival data is used in the imaging procedure. To examine if the frequency content of the data influences the result seen in Figures 3, 4 and 5 we compute imaging results for simple model B (anhydrite present) but with the dominant frequency of the source Ricker wavelet being that of 10Hz (Figure 6).

Fold

We consider a constant surface array spread of 10km but decrease the number of receivers from 501 receivers with 20m spacing, to 101 receivers with 100m spacing and again to 51 receivers with 200m spacing. Shown in Figures 7 and 8 are the SDI and MTMI imaging results for the various array spacing scenarios. Table 1 provides a summary of the imaging

14

results in terms of location accuracy and precision.

Offset

Here we shift the centre of a 6km (61 receivers, 100m spacing) surface array laterally away from the source location. Three offsets are investigated, 0km (no offset, source directly above the centre of the array), 1km and 2km. In Figures 9 and 10 the SDI and MTMI imaging results for the three array offsets are shown. Table 1 provides a summary of the imaging results in terms of location accuracy and precision.

Multiple Reflected Energy

To explore the influence of non-discrete velocity transitions, we consider three velocity models which differ in terms of the degree of smoothing applied prior to generating the synthetic waveforms. Smoothing the velocity model results in a first-order continuous velocity gradient rather than discrete discontinuities in velocity and so reduces the influence of non-primary energy seen within the data.

Two different velocity models are created via smoothing the original sonic log data (model D) leaving us with an original unsmoothed velocity model and two smoothed profiles. To smooth the original sonic log, it is first converted into slowness (to preserve the time-depth relationship) and then smoothed via convolving the slowness field with a spatial Gaussian window,

$$w(n) = exp[-\frac{1}{2}\frac{\alpha n}{N/2}], \tag{1}$$

where the standard deviation is $\sigma = N/(2\alpha)$, n the sample point, N the total number of samples and α a constant. The smoothed slowness field is then converted back to velocity.

The extent of smoothing is controlled by the width, σ, of the Gaussian filter. A moderately smoothed model is created with Gaussian window of $\sigma = 10$ and a strongly smoothed model with Gaussian window of $\sigma = 2$. We include attenuation within each model and use a source with a dominant frequency of 100Hz. The length of the array is kept constant at 10km, but we make use of only 101 receivers at 100m spacing. Shown in Figure 11 are the velocity models and their respective vertical (z) component microseismic waveforms. Figure 12 displays the SDI and MTMI imaging results for each model. While in Figure 13, snapshots of the MTMI function are shown for both the non-smoothed and moderately smoothed velocity models. These snapshots are taken from the uncollapsed MTMI function and show the image domain stacking function at different origin times.

DISCUSSION

The results shown in the previous section suggest that a decrease in effective array aperture caused by the presence of a fast lithological layer results in elongation of image peaks in SDI, and elongation and splitting of image peaks in MTMI. Elongation of image peaks in both SDI and MTMI is a result of the amplification in origin time-depth trade off such that a poorly constrained origin time determination is causing poor vertical resolution. Correct origin time determination depends on how much of the normal moveout curvature is captured by the array aperture. The fast Anhydrite acts to reduce the effective array aperture and hence origin time is poorly determined. This is apparent in Figures 3 and 4 with Table 1 numerically justifying this claim by highlighting the degradation in precision in Δz.

It should be noted that the improvement in precision seen in the SDI results in Table (1) for simple model B is unexpected and could potentially present an interesting topic for

further research. However, the degradation in accuracy of the location estimation (increase in location bias of 43m for the 4km spread when anhydrite is present) and an evident nosier image domain with increased smearing, suggests this unexpected result be an artifact of post-processing. As aperture is reduced and ray angles tend more towards vertical, image peaks become increasingly thinner and domain noise and smearing gets compressed. Very thin image peaks, a result of using a small aperture on exact synthetic data, will get suppressed via the application of the 2D spatial filter which may also be aided by the coming together of close neighboring noise peaks.

The splitting of image maxima in the MTMI domain is known as *leakage* and is caused by an imbalance in the individual moment tensor image functions where the given data can be modelled as either a single component of the moment tensor or simultaneous but spatially separate sources acting on different, incorrect components (e.g., Chambers et al., 2014).

To reduce leakage, S-wave data can be incorporated into the MTMI process. The results shown in Figure 5 demonstrate the improvement in image quality when using both P- and S-wave energy as multiple peaks converge to a single maxima. For example, taking model D we can see a significant improvement in both event location accuracy (reduction in location bias from 62m to 12m) and precision (reduction in Δy from 92m to 40m and similar Δz from 210m to 216m). This convergence and improvement in precision is also mimicked by the simple model example but an increase in location bias is seen from 72m to 100m. This increase in location bias is due to incorporating a smoothed S-wave velocity model into the imaging procedure. The accuracy of the SDI and MTMI procedures is strongly dependant on the computed travel time tables from ray tracing. For ray tracing a sufficiently smoothed velocity model is required. The smoothing of a velocity model effectively alters

its true shape and thus introduces error into the imaging procedure, significantly impacting event location. Therefore incorporating a smoothed S-wave velocity model into the imaging process increases this error and therefore it should be emphasised that the use of S-wave data in the imaging procedure requires an accurate S-wave velocity model otherwise imaging results can be degraded.

Figure 6 demonstrates that imaging on lower frequency data accentuates the elongation of image peaks and increases leakage in MTMI to an extent that even P- and S-wave imaging cannot suppress. Therefore the effects caused by anhydrite or fast velocity layers is accentuated for lower frequency data as a broader wavelet increases the coherency of the event when aligned on neighbouring image points close to the actual source location

It can be observed that decreasing the number of receivers does not have a significant effect on the location bias (i.e., differences in error of < 15m) or precision (i.e., differences of < 150m in both the y and z) of the estimated event locations. These results are seen due to the lack of coherent noise within the synthetic data. It is this coherent noise which could produce multiple maxima in the image domain and determining the primary peak would require greater fold of cover. However, realistic coherent noise, characteristic of a surface microseismic scenario is practically impossible to model without access to actual recorded noise.

As the the centre of the array is moved further away from the microseismic event, the image domain becomes increasingly smeared as peaks are elongated and skewed (see Figures 9 and 10). The amount of smearing seems to increase when anhydrite is present while the angle of smearing appears to decrease. This is considered to be the result of the different incident ray angles on the source image point, as the presence of anhydrite refracts ray

paths closer to the vertical. Although reviewing the results in Table 1 suggest no simple relationship between location bias and precision (e.g. Improvement of 95m location bias is recorded for array offset of 2km, going from no anhydrite model C, to anhydrite, model D, yet a degradation in location precision of 239m in y and 436m in z is seen), qualitatively evaluating the results in Figures 3 and 4 it is evident that the presence of anhydrite decreases the resolution of the image domain reducing one's confidence in the numerical results.

The reduction in impedance contrast as a result of smoothing the complex velocity model results in a decrease in visible non-primary energy within the synthetic seismograms (Figure 11). The SDI results from this data clearly show how this non-primary energy maps onto image points directly below the true event location These multiple maxima are a result of coherent, non-primary energy arriving later than the event first arrivals but with a comparable move out. The effects of the non-primary energy are not initially as apparent in the final MTMI results. However, analysing the MTMI image domain at various origin times in Figure 13, we can clearly see the focussing of this non-primary energy, onto deeper image points later in time. The true source origin time in this respect is t=0.435 seconds where we can clearly see a focussing of energy for both the smoothed and unsmoothed model. However, the unsmoothed model MTMI result also shows the focussing of other events at deeper image points with origin time t=0.5 seconds, which correspond to the non-primary (multiple) energy mapping to the MTMI image domain. These secondary peaks are suppressed when collapsing the MTMI image in time due to the significantly greater amplitude of the true peak. Secondary peaks are then suppressed even more by the application of a spatial Gaussian filter to the 2D collapsed image.

It should be noted that the MTMI final image function shown in this study are the sum of squares of the individual moment tensor MTMI image functions. Therefore secondary

peaks caused by these multiple events apparent in the individual moment tensor image domains are suppressed when squared and summed to produce the final MTMI stack.

By reducing our model from 3D to 2D, the incorrectly modelled geometrical spreading influences the computed amplitudes. Thus it is expected that the reduction to 2D will lead to overestimates of both primary and scattered wave amplitudes. To justify that our conclusions are still valid for 3D problems, we analyse imaging results from a 3D model using the FD algorithm of Xu (2011). The 3D forward model has a similar monitoring scenario (100m geophone spacing), but for a point compressional source (Sobion, 2014). The P- and S-wave velocity models are shown in Figure 14 along with x and y slices of the SDI and MTMI imaging volumes. The dimensions of the monitoring volumes (in x, y, z) for the simple and the complex 1D velocity model are $4.0 \times 4.0 \times 3.0 \text{km}^3$ and $7.0 \times 7.0 \times 3.0 \text{km}^3$, respectively. The source locations for the simple and complex models are $x = y = 2.0 \text{km}$ and $z = 1.2 \text{km}$, and $x = y = 3.5 \text{km}$ and $z = 2.5 \text{km}$, respectively. The density profile is not shown but is calculated using the relationship of Gardner et al. (1974). For the 3D synthetic data, the identical post-processing workflow is applied to each image function as was done with the 2D synthetic data. The results suggest that even using 3D simulation and correctly modelled geometrical spreading, non-primary energy can leak into the image domain. Although these amplitudes are smaller in magnitude, they still stack and leak into the final result. Both SDI and MTMI imaging results possess faint secondary maxima directly below the source location, with the simple model results producing more distinct secondary peaks due to the more extreme velocity transitions. Note that since the source mechanism for the 3D simulation is a compressional point source and not a double-couple source, the lobes for the SDI image are not present.

CONCLUSIONS

The main aims of this study were to understand why previous imaging results in sub-salt scenarios were of poorer quality than normal scenarios by examining the imaging difficulties due to a reduction in effective array aperture and increased coda within microseismic data caused by the presence of a fast anhydrite layer. To accomplish this, we generate finite-difference, full waveform microseismic synthetics derived from one-dimensional sonic log data taken from an unconventional shale reservoir in complex anhydrite geology. The relatively noisy signals seen in the more complex models mimic actual sub-salt microseismic datasets, which lends credibility to these relatively noise free synthetic waveforms. We then compare microseismic imaging results computed using two different imaging algorithms, a simplistic and easily reproducible Standard Diffraction Imaging (SDI) procedure and the more sophisticated Moment Tensor Microseismic Imaging (MTMI).

The results show that a fast velocity layer, in this case anhydrite, can reduce the effective aperture of surface arrays, which in turn leads to a reduction in image resolution. This is heightened when imaging with low frequency first arrival data. Both the simple SDI and sophisticated MTMI are equally affected by the presence of high velocity layers, with similar increase in location bias and degradation in precision seen in both sets of results when anhydrite is present.

Direct comparison of techniques for similar monitoring scenarios show the more sophisticated MTMI to be less affected by the presence of the anhydrite layer, generating imaging results of greater accuracy and precision. For simple SDI, the non-primary energy leaks into the image domain by converging on image points directly below the true source location. For the MTMI process, the influence of non-primary energy is less problematic due to the

final image being a sum of squares of other moment tensor MTMI image functions. However, even though suppressed, they still appear to leak into the image domain and could be mistaken as smaller events occurring with a more recent origin time.

The general recommendation is that industry should adopt larger surface arrays in basins which contain high velocity lithological units. Depending on the strength of expected impedance contrast, it would be beneficial to develop advanced microseismic processing techniques to reduce multiple and mode converted energy. This study also demonstrates that more advanced techniques are also succeptable to fast layer artifacts and can cause similar numerical instabilities, such as *'leakage'* in MTMI. Extension of this research should include investigation into the influence of layer thickness and evaporate density variations.

ACKNOWLEDGMENTS

REFERENCES

Alford, R., K. Kelly and D. Boore, D, 1974, Accuracy of finite-difference modeling of the acoustic wave equation, Geophysics, **39**, 834-842.

Angus, D.A., A. Aljaafari, P.J. Usher and J.P. Verdon, 2014, Seismic waveforms and velocity model heterogeneity: towards full-waveform microseismic location algorithm, Journal of Applied Geophysics, **111**, 228-233.

Anikiev D., F. Staněk, J. Valenta and L. Eisner, 2014, Joint location and source mechanism inversion of microseismic events: benchmarking on seismicity induced by hydraulic fracturing, Geophysical Journal International, ggu126.

Artman, B., I. Podladtchikov and B. Witten, 2010, Source location using time-reverse imaging, Geophysical Prospecting, **58**, 861-873.

Baig, A and T. Urbancic, 2010, Microseismic moment tensors: A path to understanding frac growth, The Leading Edge, **29**, 320-324.

Benson, R. and T. Davis, 2000, Time-lapse seismic monitoring and dynamic reservoir characterisation central vacuum unit lea county New Mexico, SPE Reservoir Evaluation & Engineering, **3**(01), 88-97.

Börner, K., 2003, Evaporite basins with emphasis on the permian zechstein. Oberseminar.

Campbell, C., 1987, Stratigraphy and facies of the upper elk point subgroup, northern Alberta, CSPG Special Publications, 243-286.

Chambers, K., B.D.E. Dando, G.A. Jones, R. Velasco and S.A. Wilson, 2014, Moment Tensor Migration Imaging, Geophysical Prospecting, **62**(4), 879-896.

Chambers, K., J. Kendall, S. Brandsberg-Dahl and J. Rueda, 2010, Testing the ability of surface arrays to monitor microseismic activity, Geophysical Prospecting, **58**, 821-830.

Christie-Black, N. and N.W. Driscoll, 1995, Sequence stratigraphy. Annual Review of Earth and Panetary Sciences, **23**, 451-478.

Claerbout, J.F., 1982, Imaging the earth's interior.

Drew, J., R.S. White, F. Tilmann and J. Tarasewicz, 2013, Coalescence microseismic mapping, Geophysical Journal International, **195**, 1773-1785.

Duncan, P.M., 2005, Is there a future for passive seismic?, First Break, **23**, 111-115.

Duncan, P.M. and L. Eisner, 2010, Reservoir characterization using surface microseismic monitoring, Geophysics, **75**, A139-A146.

EIA, 2013, Technically recoverable shale oil and shale gas resources: An assessment of 137 shale formations in 41 countries outside of the United States.

Einser, L., D. Gei, M. Hallo, I. Opršal and Y. Mohammed, 2013, The peak frequency of direct waves for microseismic events, Geophysics, **78**(6), A45-A49.

Eisner, L., S. Williams-Stroud, A. Hill, P. Duncan and M. Thornton, 2010, Beyond the dots in the box: Microseismicity-constrained fracture models for reservoir simulation, The Leading Edge, **29**, 326- 333.

Gajewski, D. and E. Tessmer, 2004, Reverse modelling for seismic event characterization, Geophysical Journal International, **163**, 276-284.

Gardner, G., L. Gardner and A. Gregory, 1974, Formation velocity and density-the diagnostic basics for stratigraphic traps, Geophysics, **39**, 770-780.

Gibowicz, S. J. and A. Kijko, 1994, An introduction to mining seismology, Academic Press San Diego.

Jost, M. and R. Herrmann, 1989, A student's guide to and review of moment tensors, Seismological Research Letters, **60**, 37-57.

Kelly, K., R. Ward, S. Treitel and R. Alford, 1976, Synthetic seismograms: a finite-difference approach, Geophyiscs, **41**, 2-27.

Kochnev, V.A., I.V. Goz, V.S. Polykov, I.S. Murtayev, V.G. Savin, B.K. Zommer and I.V. Brysin, 2007, Imaging hydraulic fracture zones from surface passive microseismic data, First Break, **25**, 77-80.

Larsen, S. and D. Harris, 1993, Seismic wave propagation through a low-velocity nuclear rubble zone, Lawrence Livermore National Laboratories.

Liner, C.L., 2004, Elements of 3D Seismology, PennWell.

Mapstone, N. and D. Mcilroy, 2006, Ediacaran fossil preservation: Taphonomy and diagenesis of a discoid biota from the amadeus basin, central Australia. Precambrian Research, **149**(3), 126-148.

McMechan, G.A., 1982, Determination of source parameters by wavefield extrapolation, Geophysical Journal International, **71**, 613-628.

O'Toole, T.B. and J.H. Woodhouse, 2011, Numerically stable computation of complete synthetic seismograms including the static displacement in plane layered media, Geophysical Journal International, **187**, 1516-1536.

Ózbek, A., T. Probert, D. Raymer and J. Drew, 2013, Nonlinear Processing Methods for Detection and Location of Microseismic Events, 75th EAGE Conference & Exhibition incorporating SPE EUROPEC.

Price, D., 2013, The effect of anhydrite on the surface imaging of microseismic events, M.Sc. dissertation, University of Leeds.

Robein, C., F. Drapeau, D. Maurel, E. Gaucher and E. Auger, 2009, Multi-network microseismic monitoring of fracturing jobs: Neuquen TGR application, 71st Conference & Technical Exhibition, **X009**.

Šílený, J., 2009, Resolution of non-double-couple mechanisms: Simulation of hypocenter mislocation and velocity structure mismodeling, Bulletin of the Seismological Society of America, **99**, 2265-2272.

Sloss, L., 1959, Relationship of primary evaporites to oil accumulation. 5th World Petroleum Congress, World Protroleum Congress.

Sobion, C., 2014, The effect of anisotropy on the surface imaging of microseismic events, M.Sc. dissertation, University of Leeds.

Trifu, C.I., D.A. Angus and V. Shumila, 2000, A Fast Evaluation of the Seismic Moment Tensor for Induced Seismicity, Bulletin of the Seismological Society of America, **90**, 1521-1527.

Udías Vallina, A., 1999, Principles of seismology, Cambridge University Press.

Vavryčuk, V., 2007, On the retrieval of moment tensors from borehole data, Geophysical Prospecting, **55**, 381-391.

Warpinski, N., 2009, Microseismic monitoring: Inside and out, Journal of Petroleum Technology, **61**, 80-85.

Warpinski, N., M. Mayerhofer, A. Bridges and J. DU, 2012, Hydraulic Fracture Geomechanics and Microseismic Source Mechanisms, SPE Annual Technical Conference and Exhibition.

Waters, K.H., 1978, Reflection Seismology: A tool for energy resource exploration.

Xuan, R. and P. Sava, 2010, Probabilistic microearthquake location for reservoir monitoring, Geophysics, **75**, MA9-MA26.

Yilmaz, Ö. and S.M. Doherty, 1987, Seismic data processing, Society of Exploration Geophysicists Tulsa.

Xu, Y., 2011, Analysis of P-wave seismic response for fracture detection: modelling and case studies, PhD dissertation, University of Edinburgh.

		MTMI				SDI	
		Location Bias	Precision			Location Bias	Precision
Model	Aperture (km)	Error (m)	Δy (m)	Δz (m)	Error (m)	Δy (m)	Δz (m)
A	10	0.14	26.50	87.10	39.20	394.00	325.00
	6	12.37	43.70	107.00	39.14	369.00	482.00
	4(P)/4(P+S)	12.46/12.53	76.10/35.70	151.00/86.50	39.51/NA	474.00/NA	808.00/NA
	4(10Hz, P)/4(10Hz, P+S)	206.11/115.17	471.00/174.00	796.00/263.00	223.61/NA	670.00/NA	1550.00/NA
B	10	62.52	36.40	146.00	44.60	488.00	853.00
	6	25.02	72.20	169.00	52.70	111.00	301.00
	4(P)/4(P+S)	72.12/100.00	92.40/40.50	183.00/111.00	83.79/NA	202.00/NA	831.00/NA
	4(10Hz, P)/4(10Hz, P+S)	206.17/485.40	524.00/284.00	1400.00/897.00	215.77/NA	830.00/NA	1760.00/NA
C	10	62.44	31.50	96.00	118.56	127.00	244.00
	6	62.47	62.30	105.00	130.48	154.00	1170.00
	4(P)/4(P+S)	67.41/74.95	85.50/27.40	143.00/144.00	789.97/NA	180.00/NA	1190.00/NA
D	10	0.10	60.00	110.00	53.09	136.00	1030.00
	6	35.14	84.50	136.00	237.74	141.00	1130.00
	4(P)/4(P+S)	62.14/12.45	100.00/36.10	210.00/216.00	900.80/NA	180.00/NA	1250.00/NA

		MTMI				SDI	
		Location Bias	Precision			Location Bias	Precision
Model	Spacing (m)	Error (m)	Δy (m)	Δz (m)	Error (m)	Δy (m)	Δz (m)
A	20	0.08	25.60	87.10	25.96	347.00	280.00
	100	0.14	26.50	87.10	39.20	394.00	325.00
	200	0.19	28.50	87.40	25.67	476.00	384.00
B	20	50.00	63.80	176.00	44.45	381.00	739.00
	100	62.52	63.40	146.00	44.61	488.00	853.00
	200	50.08	63.80	176.00	44.47	343.00	876.00
C	20	62.39	31.50	96.10	118.53	128.00	239.00
	100	62.44	31.50	95.60	118.56	127.00	244.00
	200	62.50	29.90	94.80	106.78	126.00	245.00
D	20	0.16	56.70	115.00	53.13	135.00	992.00
	100	0.10	60.00	110.00	53.09	136.00	1030.00
	200	0.09	52.50	107.00	53.01	136.00	1060.00

		MTMI				SDI	
		Location Bias	Precision			Location Bias	Precision
Model	Offset (km)	Error (m)	Δy (m)	Δz (m)	Error (m)	Δy (m)	Δz (m)
A	0	12.37	43.70	107.00	39.14	369.00	482.00
	1	0.11	67.30	120.00	62.70	340.00	464.00
	2	17.64	165.00	251.00	80.06	296.00	348.00
B	0	62.52	72.20	169.00	52.70	111.00	301.00
	1	252.89	197.00	624.00	106.88	339.00	1160.00
	2	288.48	174.00	531.00	276.66	427.00	1210.00
C	0	62.47	62.30	105.00	130.48	154.00	1170.00
	1	50.03	120.00	206.00	154.64	183.00	1190.00
	2	134.52	177.00	289.00	182.03	210.00	1140.00
D	0	35.14	84.50	136.00	242.63	141.00	1130.00
	1	72.60	170.00	376.00	118.71	157.00	1180.00
	2	39.55	416.00	725.00	146.31	304.00	1250.00

Table 1: Numerical results for (Top) Aperture experiment (Figures 3 to 6) (Middle) Receiver spacing (Figures 7 to 8) and (Bottom) Offset experiments (Figures 9 to 10). Location bias being a measure of distance between estimated source location and actual known location (given to sub meter precision due to exact nature of synthetic data). Precision being a measure, along the two axes, of the 75% contour of the normalised image function i.e size of contoured surface in y and z.
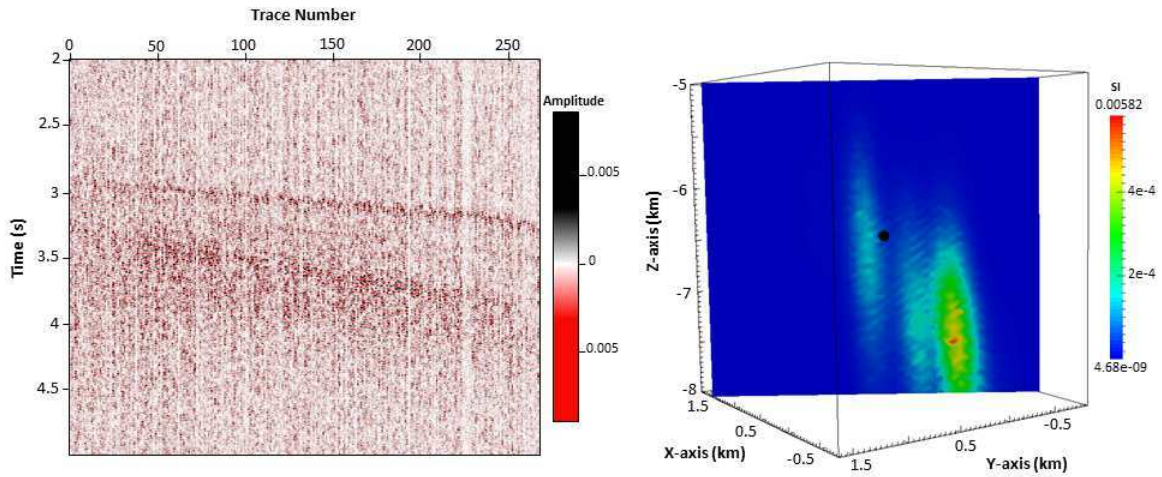
Figure 1: Left: pre-processed vertical component surface array microseismic data. P-wave first arrival is followed by multiply reflected and converted coda related to the presence of anhydrite. Right: MTMI imaging result of a perforated microseismic event with known event location (black dot). A noisy and multi-ellipsoidal diffuse coherence pattern in the image domain has led to an estimated source location having vertical and lateral errors of approximation 1km and 200m, respectively (Figure published with permission from Pinnacle-a Halliburton Service).

28
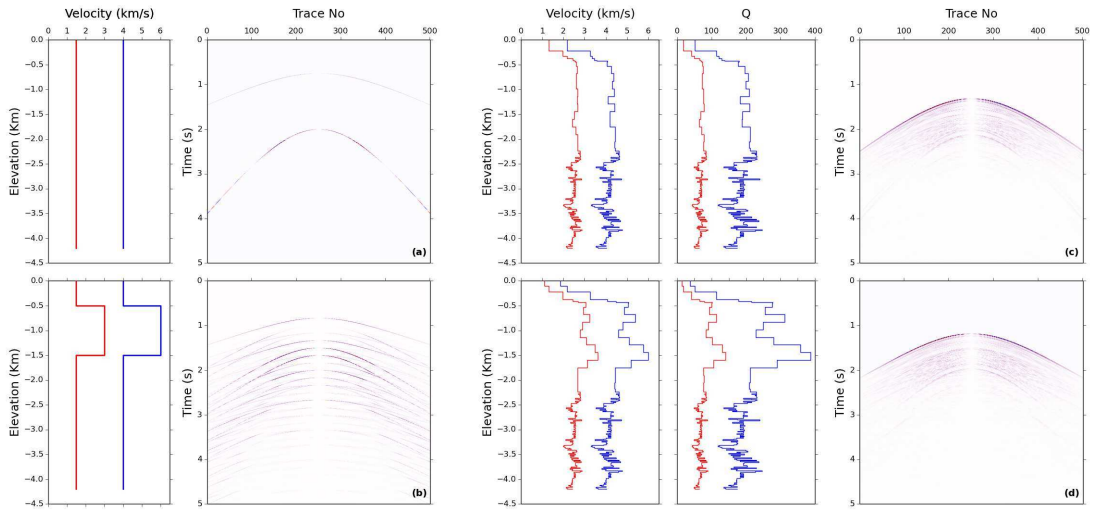
Figure 2: Velocity models (P-wave = blue line and S-wave = red line) with their respective vertical (z) component microseismic waveforms: (a) Simple model A, (b) Simple model B, (c) Complex model C, and (d) The actual unconventional sonic log, complex model D.
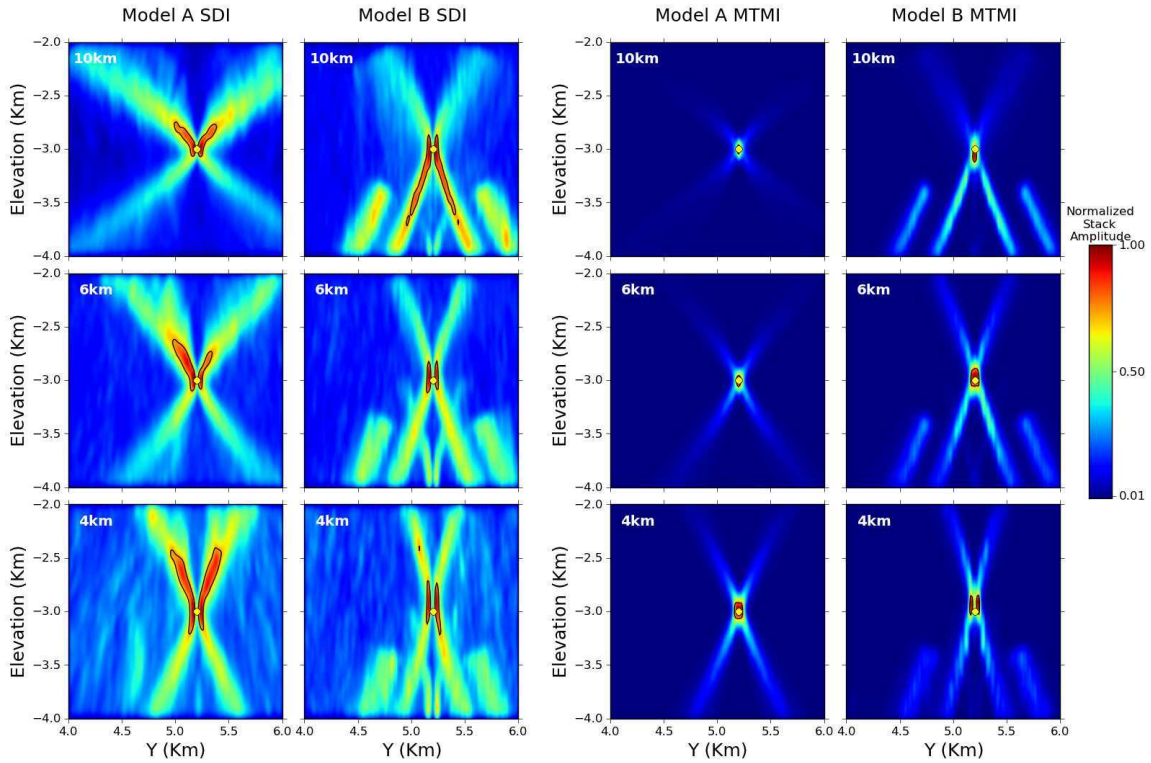
Figure 3: Comparison of microseismic imaging due to variable aperture. Results show SDI and MTMI image functions for 10km, 6km and 4km arrays for simple models A and B. All images are normalised with respect to the maximum scalar and are collapsed in origin time showing only the maximum stacking value for each image point. The true source location is shown by the yellow dot, and the 75% error contours are shown by the black lines.
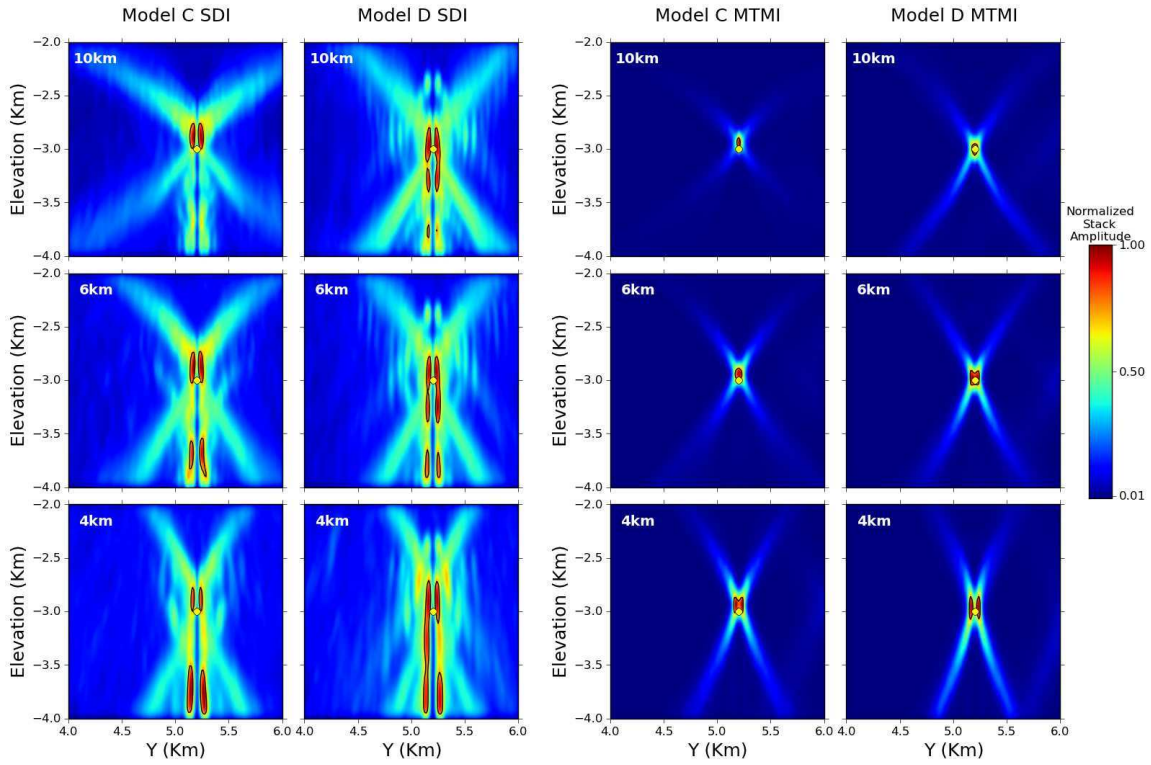
Figure 4: Comparison of microseismic imaging due to variable aperture. Results show SDI and MTMI image functions for 10km, 6km and 4km arrays for complex models C and D. All images produced using the same procedure as that for Figure 3.
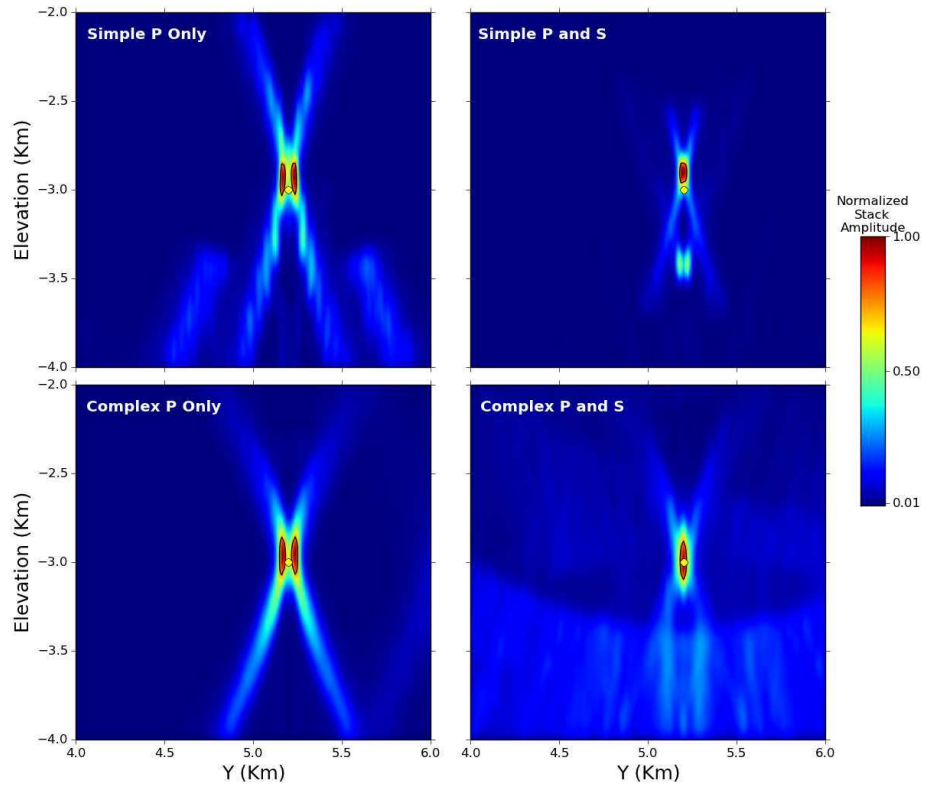
Figure 5: MTMI image functions computed for simple model B and complex model D using P-wave energy only (left) and P- and S-waves energy (right) for the 4km spread array. All images produced using the same procedure as that for Figure 3.
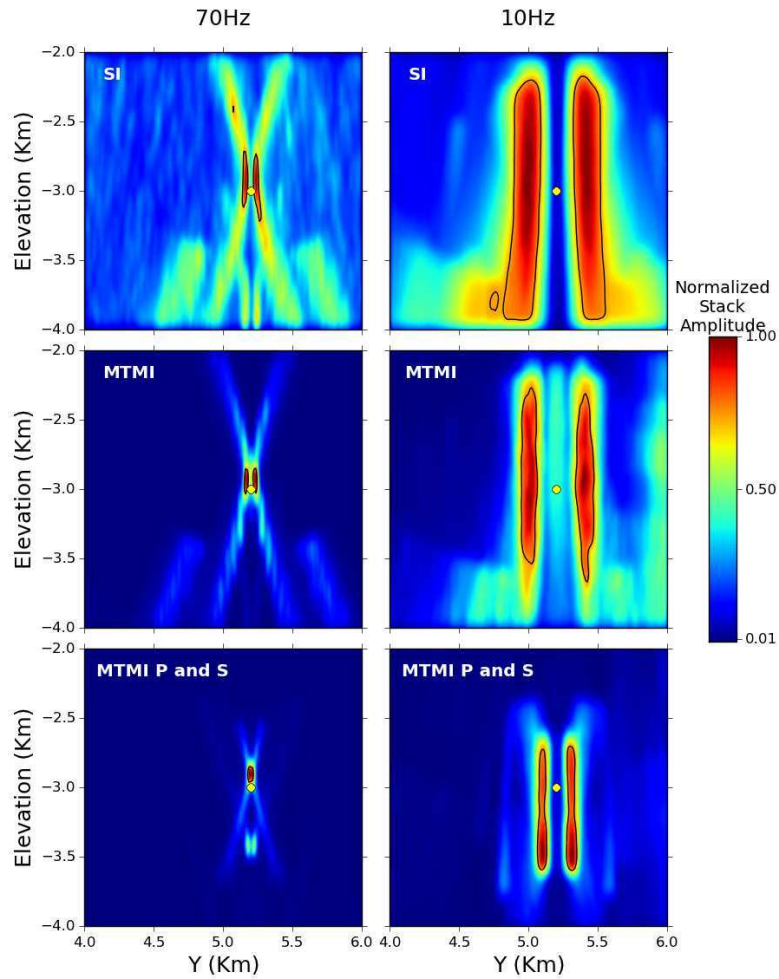
Figure 6: SDI and MTMI image functions computed for simple anhydrite model B when dominant frequency of microseismic event is (left) 70Hz and (right) 10Hz. Images are computed using an array length of 4km with 100m receiver spacing. Results are presented for SDI, MTMI P-wave only imaging and MTMI P- and S-wave imaging. All images produced using the same procedure as that for Figure 3.
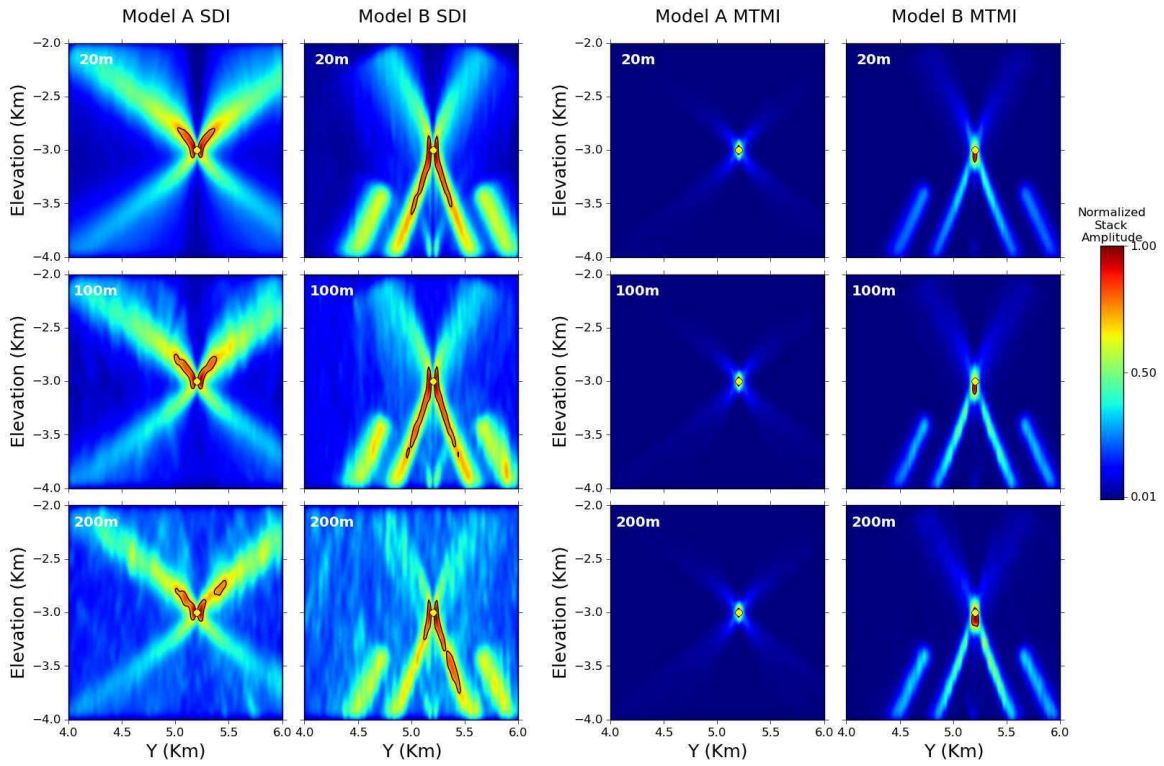
Figure 7: Comparison of microseismic imaging due to variable receiver spacing. Results show SDI and MTMI image function for receiver spacings of 20m, 100m and 200m for simples models A and B. All images produced using the same procedure as that for Figure 3.
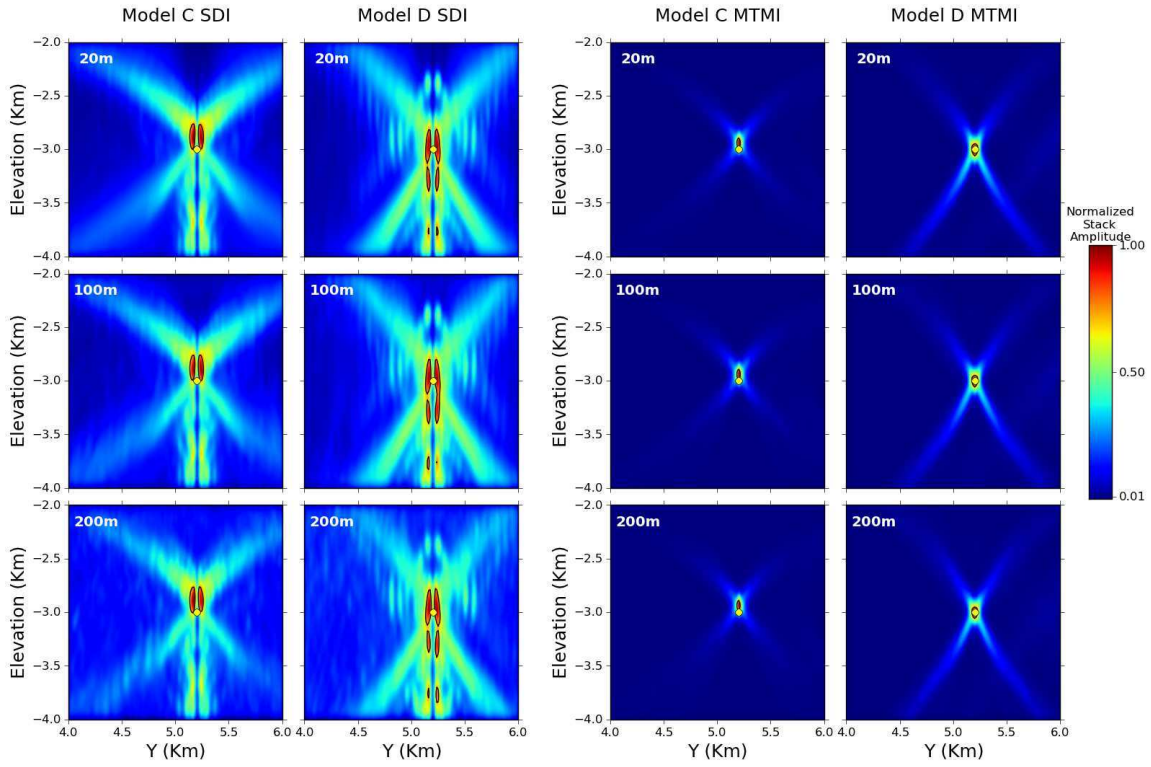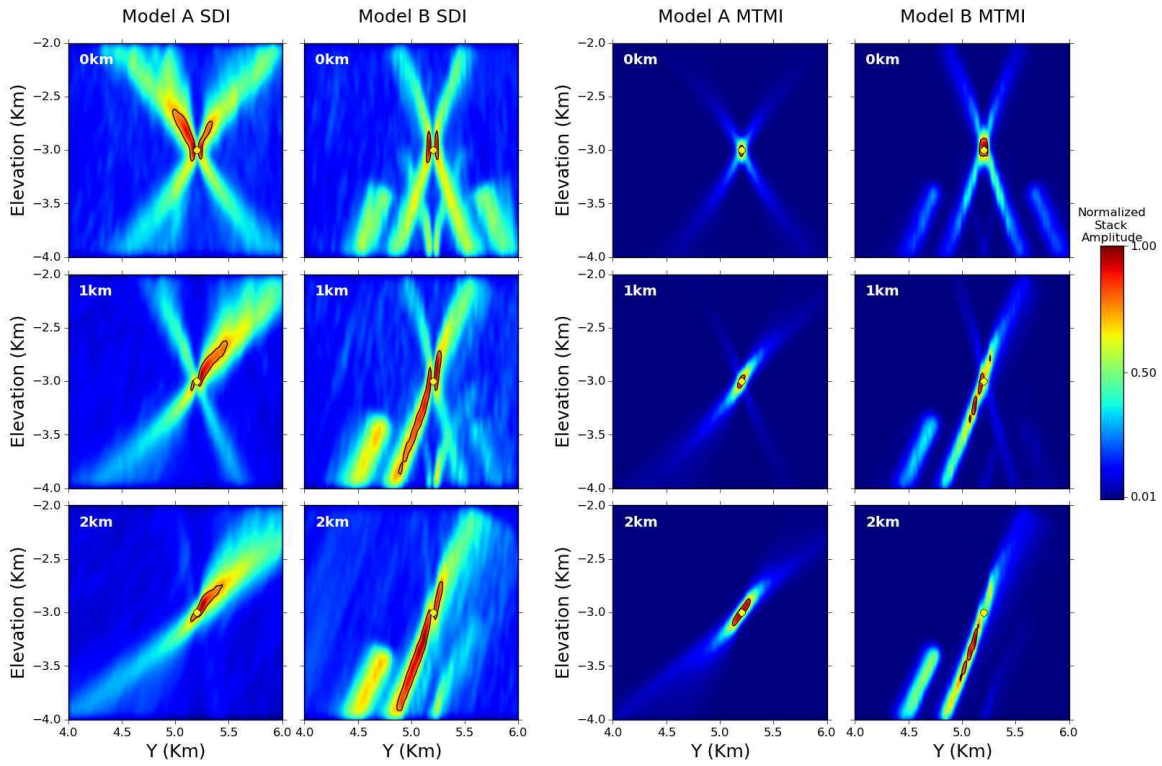
Figure 8: Comparison of microseismic imaging due to variable receiver spacing. Results show SDI and MTMI image function for recever spacings of 20m, 100m and 200m for complex models C and D. All images produced using the same procedure as that for Figure 3.
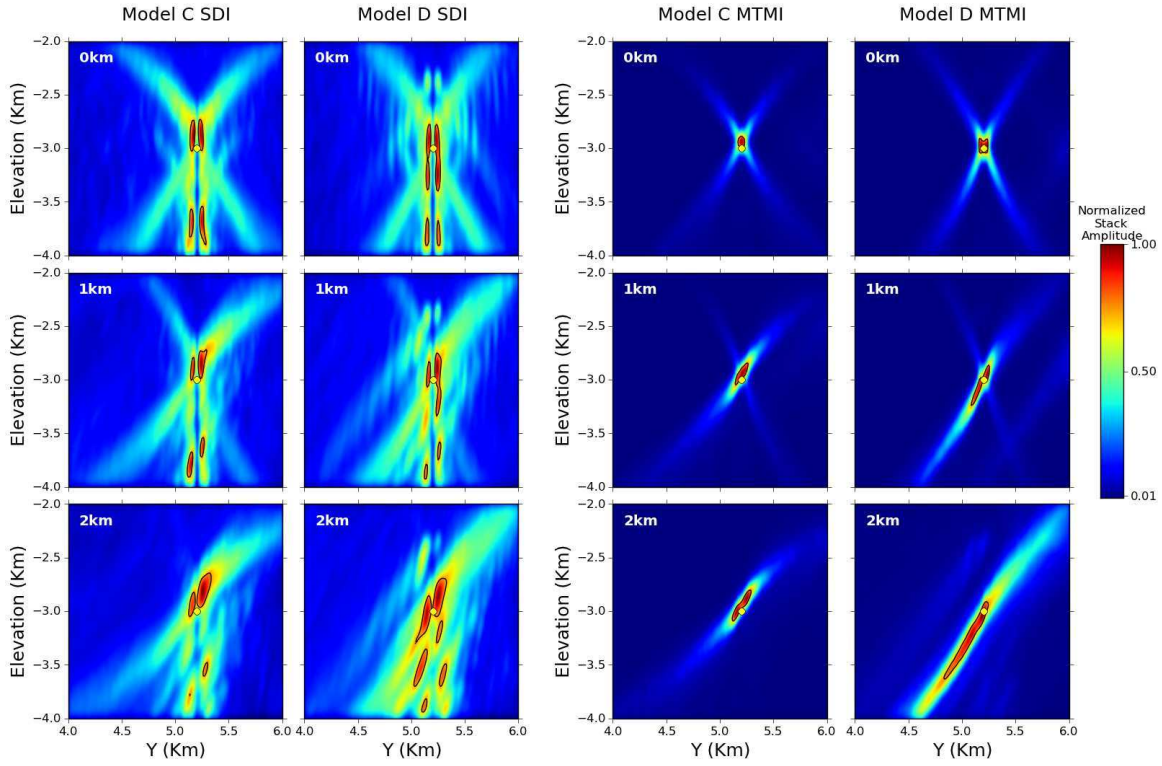
Figure 9: Comparison of microseismic imaging due to variable source offset. Results show SDI and MTMI image function for source offset of 0km, 1km and 2km from the centre of the array for simple models A and B. Total array length of 6km used for this test with 100 receiver spacing. All images produced using the same procedure as that for Figure 3.
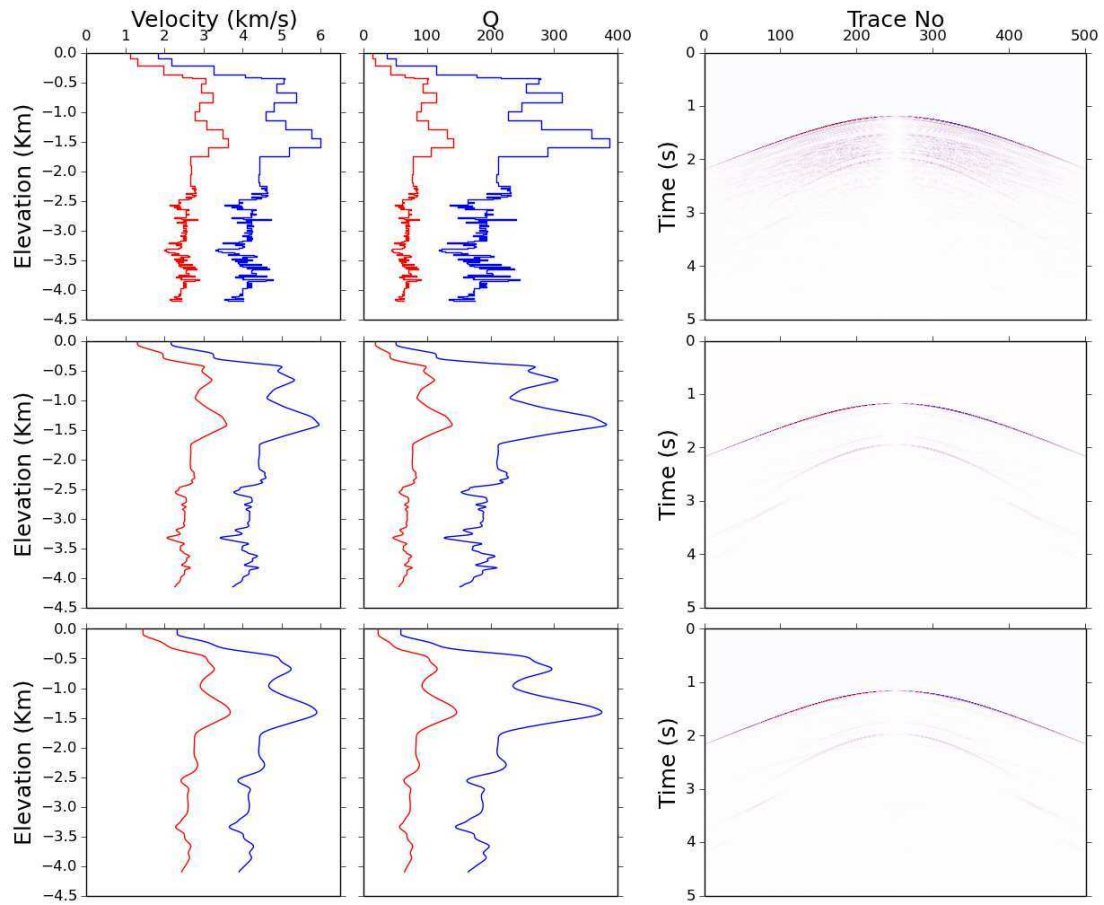
Figure 10: Comparison of microseismic imaging due to variable source offset. Results show SDI and MTMI image function for source offset of 0km, 1km and 2km from the centre of the array for complex models C and D. Total array length of 6km used for this test with 100 receiver spacing. All images produced using the same procedure as that for Figure 3.

Figure 11: Velocity models (P-wave = blue line and S-wave = red line) with their respective vertical component microseismic waveforms.
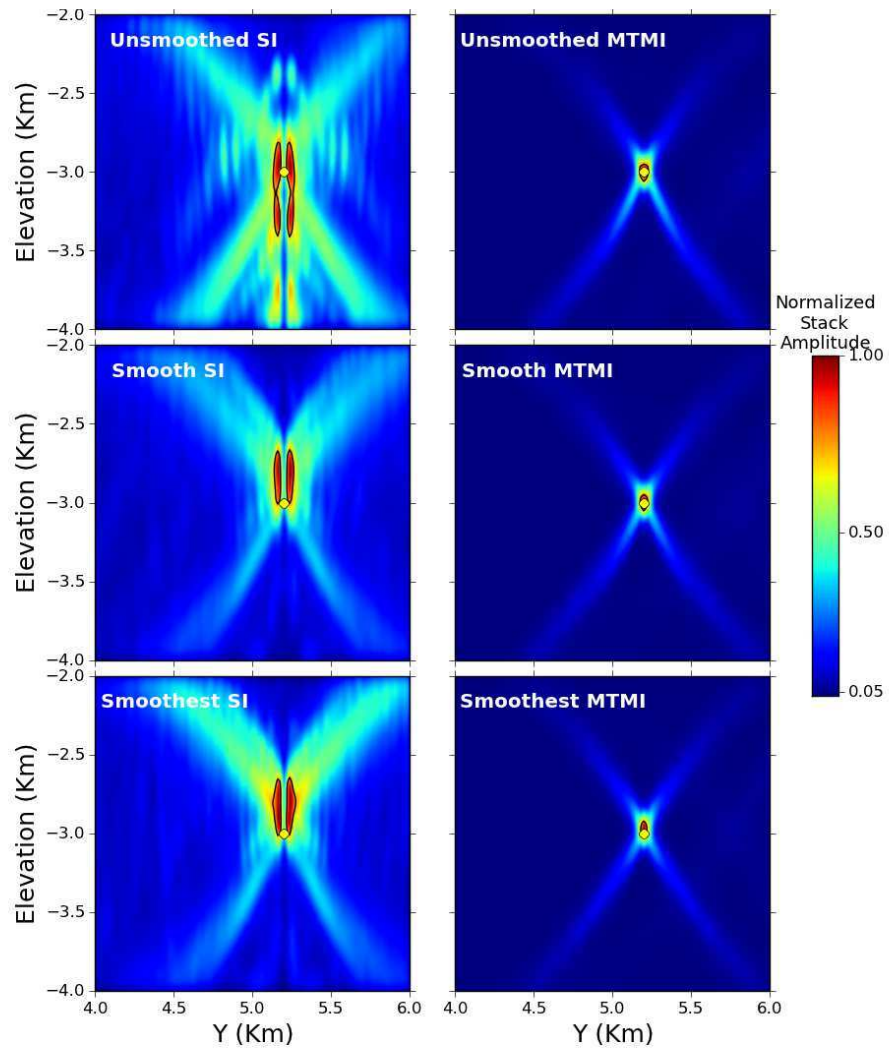
Figure 12: SDI and MTMI image functions collapsed in origin time for the velocity models shown in Figure 11
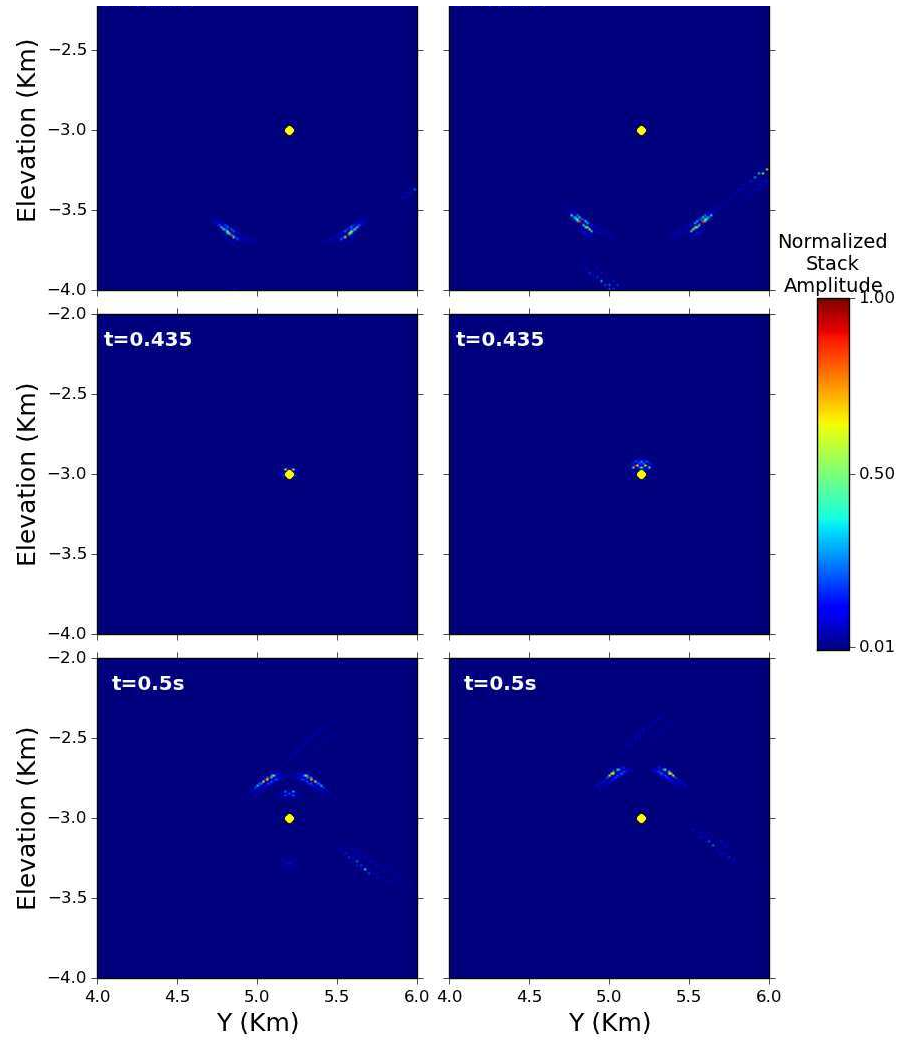
Figure 13: MTMI image functions at various origin times for the non-smoothed complex velocity model and the moderately smoothed velocity model shown in Figure 11.
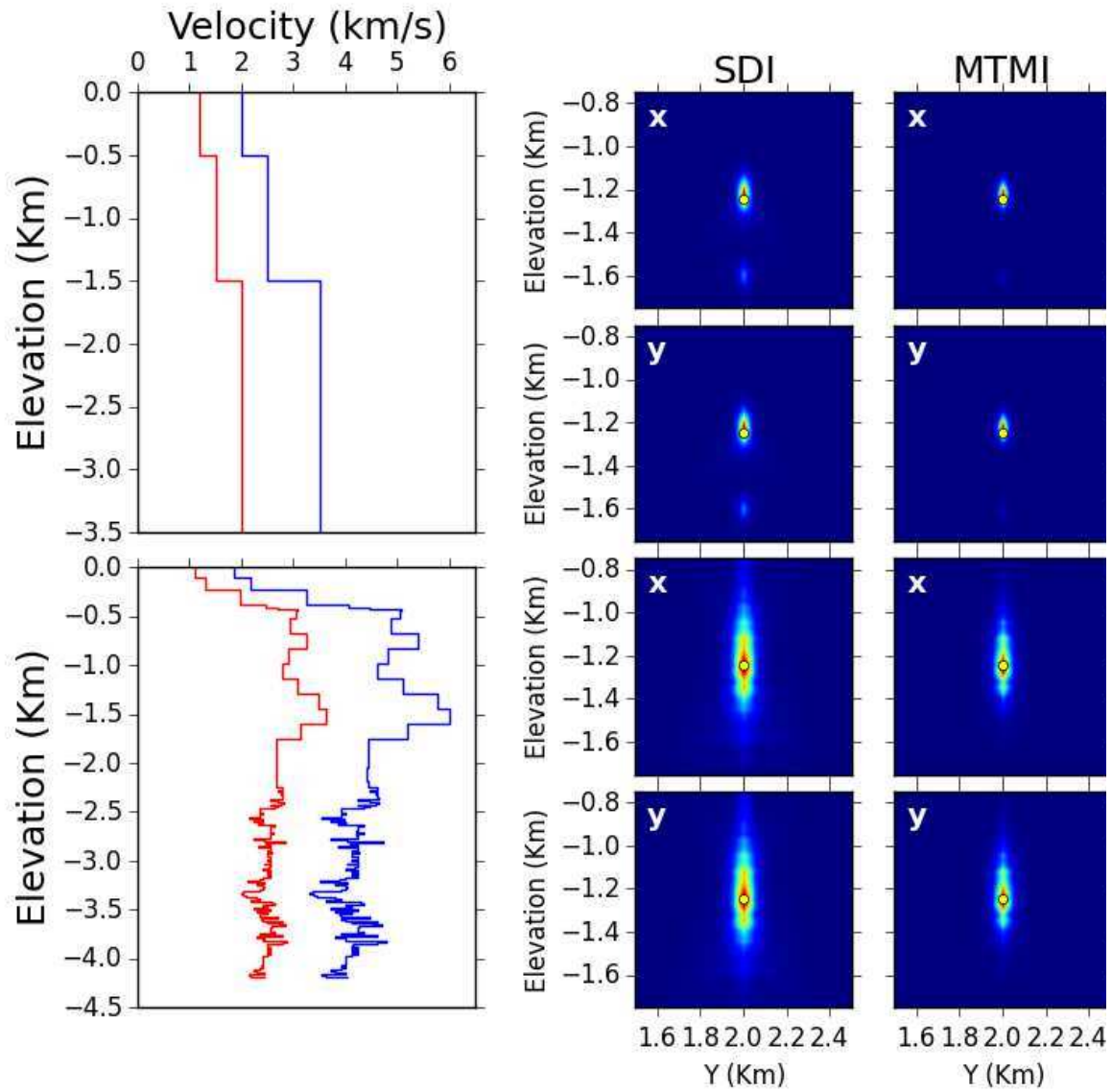
Figure 14: 1D P- (Blue) and S-wave (Red) velocity models use by Sobion (2014) to create 3D FD microseismic synthetics. Their corresponding SDI and MTMI results are shown as 2D slices of the 3D volume along x and y, taken at the source location. The actual source location is shown by the yellow dot.